3D First limits Foreground and sensitivity analysis for 21cm/Infrared intensity mapping correlation from the Epoch of Reionization

Abraham R. Neben[1], Brian Stalder[2], John L. Tonry[2], Jacqueline N. Hewitt[1]

[1]*MIT Kavli Institute, Massachusetts Institute of Technology, Cambridge, MA, 02139 USA*

[2]*Institute for Astronomy, University of Hawaii, 2680 Woodlawn Drive, Honolulu HI 96822*

ABSTRACT

aoeu

Subject headings: cosmology: observations — dark ages, reionization, first stars — infrared: diffuse background

1. Introduction

Deep radio and infrared observations are nearing detection of the first stars and galaxies from the cosmic dawn. As such sources form, they are thought to blow out ionized bubbles, eventually merging and reionizing the universe (Furlanetto et al. 2006; Morales & Wyithe 2010; Pritchard & Loeb 2012). First generation 21 cm observatories such the Murchison Widefield Array (MWA) (Tingay et al. 2013; Bowman et al. 2013) and the Precision Array for Probing the Epoch of Reionization (PAPER) (Parsons et al. 2014; Ali et al. 2015; Pober et al. 2015; Jacobs et al. 2015) are setting ever tighter limits on redshifted neutral hydrogen emission from the neutral regions between these bubbles, and the now-underway Hydrogen Epoch of Reionization Array (HERA) (DeBoer et al. 2016) is expected to detect and characterize the EOR power spectrum in the coming years. Ultimately, the Square Kilometer Array (SKA) will image the EOR over redshift, revealing the hydrogen reionization history of the universe in detail (Hall 2005).

At the same time, deeper galaxy redshift surveys are beginning to constrain the reionizing sources themselves. Hubble deep field observations (Bouwens et al. 2011; Illingworth et al. 2013; Dunlop et al. 2013) and cluster lensing surveys are finding tens of galaxies at $6 < z < 10$ down to UV magnitudes of $M_{AB} \sim -17$, and extremely wide surveys are underway aiming to find rare extremely bright ones ones (Schmidt et al. 2014; Trenti et al. 2011; Bradley et al. 2012). However, current models require the contribution of far fainter galaxies down to $M_{AB} \sim -13$ (Robertson et al. 2013; Alvarez et al. 2012) in order to agree with optical depth measurements (Planck Collaboration et al. 2016) from the cosmic microwave background. Deeper observations with the James Webb Space Telescope (JWST) (Gardner et al. 2006) and the Wide Field Infrared Space Telescope (WFIRST) (Spergel et al. 2013) will be needed to probe this crucial faint population (Atek et al. 2015).

Infrared intensity mapping offers several advantages compared to surveys. Power spectrum analyses can be sensitive to an EOR component even if the signal-to-noise in individual pixels small, and instead of being limited to the brightst galaxies, intensity mapping is sensitive to the cumulative light from *all* sources. Indeed, ionizing and Lyman-alpha radiation from EOR galaxies at $z \sim 6-8$ redshifts into the near infrared, motivating intensity mapping at micron-scale wavelengths. Working around foregrounds is challenging, though. While early studies suggested angular fluctuations in infrared intensity maps traced EOR galaxies (e.g., Kashlinsky et al. 2005, 2007, 2012), Helgason et al. (2016) find that given current constraints on the EOR, this is unlikely. In fact, Cooray et al. (2012); Zemcov et al. (2014) argue that intrahalo light, consisting of tidally stripped stars dispersed throughout host halos, is the best explanation for the observed fluctuation excess over known galaxy populations. This implies that even after significant foreground masking, EOR foreground emission in wide field infrared surveys is of order 10^4 times brighter than EOR emission at $\sim 10'$ scales.

Given these bright foregrounds, cross correlation with 21 cm maps may in fact be the *only* way to extract the diffuse EOR component of the near infrared background. The synergy is clear: the galaxies sourcing reionization generate strong Ly-α emission, while the neutral regions between them glow at rest frame 21 cm. On scales larger than typical ionized bubbles, bright spots in IR maps likely correspond to ionized regions, and thus, 21 cm dark spots, and vice versa, sourcing an anticorrelation seen in EOR simulations by Fernandez et al. (2014); Silva et al. (2013); Mao (2014); Heneka et al. (2016).

A similar anticorrelation on large scales is found by Lidz et al. (2009); Park et al. (2014) in simulations of 21 cm cross correlation with galaxy surveys, but conducting redshift surveys both wide and deep enough to cross correlate with 21 cm maps is an challenge due to the wildly different spatial scales probed by 21 cm experiments and deep galaxy surveys. The Hubble Ultra Deep Field, for instance, could fit inside a single resolution element in an MWA map. It may be possible to cross-check the ionization environment of deep JWST sources by comparing the brightness temperature in the 21 cm map (Beardsley et al. 2015), but even after order ~ 100 hour integrations such detections will be near JWST limiting sensitivities Zackrisson et al. (2011).

In contrast, intensity allows similar science with shallower observations, though imperfect radio and infrared foreground subtraction will leak largely uncorrelated power into the cross correlation analysis which must be averaged out over large fields of view. Fortunately the planned Transiting Exoplanet Survey Satellite (Ricker et al. 2014) and the proposed SPHEREx mission (Doré et al. 2014, 2016) would collect all sky near infrared maps, and many ground-based near infrared surveys with few degree fields such as the Dark Energy Survey (Dark Energy Survey Collaboration et al. 2016), Pan-STARRS (Tonry et al. 2012), and the Asteroid Terrestrial-impact Last Alert System (ATLAS) (Tonry 2011) are coming online. In the low frequency radio, the MWA has performed a deep survey of 400 square degrees at high galactic latitude (Beardsley et al. 2016), and HERA will survey ~ 2000 square degrees along a zenith strip (Dillon et al. 2015).

With wide and deep IR and low frequency radio surveys happening now and on the horizon, we

study in this paper the real world prospects of detecting the cross correlation of diffuse 21cm and Ly-alpha emission from the EOR. We begin in Section 1 with a cross correlation analysis of radio and near infrared catalogs, setting upper limits on the level of foreground correlation, the presence of which would mask the cosmological correlation in sufficiently deep images. We then assess the correlation of faint, unresolved emission through a prototype 21cm/IR correlation analysis between wide band MWA and ATLAS images over a 10 degree field of view. After foreground subtraction and masking, we estimate typical foreground residual levels, and synthesize these with noise predictions into a sensitivity analysis for a larger scale image cross correlation experiment. We also make sensitivity predictions for a cube cross correlation experiment, quantifying the required infrared spectral resolution and taking advantage of avoidance of radio foregrounds using the "EOR window".

2. Power spectrum and correlation conventions

2.1. Power spectrum definitions

We define the 3D power spectrum $P(\vec{k})$ of the image cube $I(x, y, z)$ following Ewall-Wice et al. (2014) as

$$P(\vec{k}) = \frac{\langle|\tilde{I}(\vec{k})|^2\rangle}{V} \tag{1}$$

where

$$\tilde{I}(\vec{k}) = dV \sum_{\vec{x}} I(\vec{x}) e^{i\vec{k}\cdot\vec{x}} \tag{2}$$

and V is the survey volume, and dV is the voxel size.

Similarly, over narrow fields of view, the angular power spectrum C_ℓ of a 2D (e.g, broad band) image $I(\vec{\theta})$ can be shown to be approximately

$$C(\vec{\ell}) = \frac{\langle|\tilde{I}(\vec{\ell})|^2\rangle}{\Omega} \tag{3}$$

where

$$\tilde{I}(\vec{\ell}) = d\Omega \sum_{\vec{\theta}} I(\vec{\theta}) e^{i\vec{\ell}\cdot\vec{\theta}} \tag{4}$$

and Ω is the survey solid angle, and $d\Omega$ is the pixel size. Thus, we need only evaluate a fourier

transform to estimate C_ℓ over a narrow field of view. Writing this out in detail, we find[1]

$$C(\ell(a,b)) = \left\langle \left| \sum_{m,n} I(m,n) \exp\left(-\frac{2\pi i}{N}(am+bn)\right) \right|^2 \right\rangle \frac{d\theta^2}{N^2} \tag{5}$$

where $d\theta = d\theta_x = d\theta_y$ is the pixel size, $N \equiv N_x = N_y$ is number of pixels on a side of a square image, and $\ell = \sqrt{\ell_x^2 + \ell_y^2}$, where

$$\ell_x = 2\pi a/Nd\theta \tag{6}$$

$$\ell_y = 2\pi b/Nd\theta \tag{7}$$

Note that C_ℓ has the units of $[I^2 d\theta^2]$. We will generally work with the dimensionally more intuitive power spectrum $\Delta(\ell)$, given by

$$\Delta(\ell) = \sqrt{\frac{\ell^2}{2\pi} C(\ell)} \tag{8}$$

which has the same units as I because ℓ has units of 1/rad.

The 3D power spectrum is often cylindrically binned to $(k_\perp, k_\parallel)$ space where $k_\perp^2 \equiv k_x^2 + k_y^2$ represents modes perpendicular to the line of sight, and $k_\parallel = k_z$ represents modes along the line of sight. We show in Appendix B that this cylindrically binned power spectrum is related to the angular power spectrum of a broad band image (over a narrow field of view) as

$$P(k_\perp, k_\parallel = 0) = D_c^2 \Delta D_c C_{\ell(k_\perp)} \tag{9}$$

with $\ell = D_c k_\perp$, where D_c is the comoving line of sight distance to the center of the cube, and ΔD_c is the comoving depth of the cube.

2.2. Cross spectrum vs. coherence

We extend the definition of the angular power spectrum given in Eqn. 3 to the cross spectrum as

$$C_{A,B}(\vec{\ell}) = \frac{\langle \tilde{I}_A^*(\vec{\ell}) \tilde{I}_B(\vec{\ell}) \rangle}{\Omega} \tag{10}$$

where A and B denote the 21 cm and the IR fields. The cross spectrum is a quantity which ranges between $\pm(C_A(\vec{\ell}) C_B(\vec{\ell}))^{1/2}$ depending on how correlated or anti-correlated the two fields are.

---

[1]IS IT REALLY RIGHT THAT ALL THESE PEOPLE WROTE IT UP WRONG? ARE THERE DIFFERENT NORMALIZATIONS OF Cℓ ? Note that the normalization of $d\theta^2/N^2$ has been misstated as $1/N^2$ by Zemcov et al. (2014) (Eqn. 3 of their supplement), $d\theta$ by Cooray et al. (2012) (Eqn. 1 of their supplement), and $N^2 d\ell^2/(2\pi)^2$ by Thacker et al. (2015) (Eqn. B3). Using Eqn. 6, the last form can be shown equal $1/d\theta^2$.

The cross spectrum is thus often renormalized as

$$c_{A,B}(\vec{\ell}) \equiv \frac{C_{A,B}(\vec{\ell})}{\sqrt{C_A(\vec{\ell})C_B(\vec{\ell})}} \tag{11}$$

where c is known as the coherence. The coherence quantifies the fractional correlation of the two fields, and is insensitive to a simple rescaling of either one. However, large foreground residuals afflicting either field will substantially bias the coherence towards zero (Lidz et al. 2009; Furlanetto & Lidz 2007).

3. 3D intensity mapping

NEED TO START REJIGGERING THIS SECTION

3.1. Sensitivity framework

We adapt the cross spectrum sensitivity results of Lidz et al. (2009) to our case of measuring the 21 cm–IR cross spectrum of broadband images with noise and foreground residuals.

$$\sigma^2_{21,\mathrm{IR}}(\vec{\ell}) = \frac{1}{2}[C^2_{21,\mathrm{IR}}(\vec{\ell}) + \sigma_{21}(\vec{\ell})\sigma_{\mathrm{IR}}(\vec{\ell})] \tag{12}$$

$$\sigma^2_{21}(\vec{\ell}) = [C_{21,\mathrm{cosmo}}(\vec{\ell}) + C_{21,\mathrm{fg}}(\vec{\ell}) + C_{21,\mathrm{therm}}(\vec{\ell})]^2 \tag{13}$$

$$\sigma^2_{\mathrm{IR}}(\vec{\ell}) = [C_{\mathrm{IR,cosmo}}(\vec{\ell}) + C_{\mathrm{IR,fg}}(\vec{\ell}) + C_{\mathrm{IR,shot}}(\vec{\ell})]^2 \tag{14}$$

where cosmo signifies the cosmological component of the signal from the EOR, fg signifies residual foregrounds, therm signifies thermal noise in 21 cm images, and shot signifies photon shot noise in IR images.

3.2. Broad band correlation experiment sensitivity

Though these are the general forms of these equations, we omit the thermal and photon shot noise contributions in the rest of this section, as we have shown them to be negligible in Sections **??** and **??**. We also omit the sample variance terms as they become important only in the SNR ~ 1 regime.

Now suppose we evaluate the 2D cross spectrum as in Eqn. 11, and bin it in annuli such that bin ℓ contains containing N_ℓ ℓ cells. Then the noise decreases as

$$\sigma^2_{21,\mathrm{IR}}(\ell) = \frac{\sigma^2_{21,\mathrm{IR}}(\vec{\ell})}{N_\ell} \tag{15}$$

Then substituting Eqns. 12-14 into the above equation and omitting factors of order unity, we find that the signal to noise ratio SNR(ℓ) of the measurement of cross spectrum mode ℓ is given by

$$\mathrm{SNR}(\ell) = \sqrt{2N_\ell \left(\frac{C_{21,\mathrm{cosmo}}(\vec{\ell})}{C_{21,\mathrm{fg}}(\vec{\ell})}\right)\left(\frac{C_{\mathrm{IR,cosmo}}(\vec{\ell})}{C_{\mathrm{IR,fg}}(\vec{\ell})}\right)} \tag{16}$$

Let us optimize the SNR by using only two bins, $\ell_1 = \ell_{\mathrm{max}}/4$ and $\ell_2 = 3\ell_{\mathrm{max}}/4$, where $\ell_{\mathrm{max}} = \pi/d\theta$ and the cell size is given by $d\ell = 2\ell_{\mathrm{max}}/N = 2\pi/\theta_{\mathrm{FOV}}$. Now let's derive some intuition into N_ℓ by writing it as $N_\ell = (\ell_{\mathrm{max}}/d\ell)^2 F_\ell = (\theta_{\mathrm{FOV}}/2d\theta)^2 F_\ell$, where F_ℓ is an order unity quantity equal to the fraction of all $\vec{\ell}$ cells included in bin ℓ.

$$\mathrm{SNR}(\ell) \quad = \quad XX \left(\frac{\theta_{\mathrm{FOV}}}{20^\circ}\right)\left(\frac{5'}{d\theta}\right)\left(\frac{F_\ell}{1}\right)^{1/2}\left(\frac{\alpha_{21}}{0.1}\right)^{1/2} \tag{17}$$

where the fraction of 21 cm foregrounds remaining after subtraction is given by $\alpha_{21} \equiv C_{21,\mathrm{res}}/C_{21,\mathrm{fg}}$, and the fraction of IR foregrounds removed by masking is assumed to be XXX. REMEMBER, WE CAN'T MASK OUR WAY TO THE SIGNAL BECAUSE OF THE INTRAHALO -LIGHT

3.3. 3D correlation experiment sensitivity

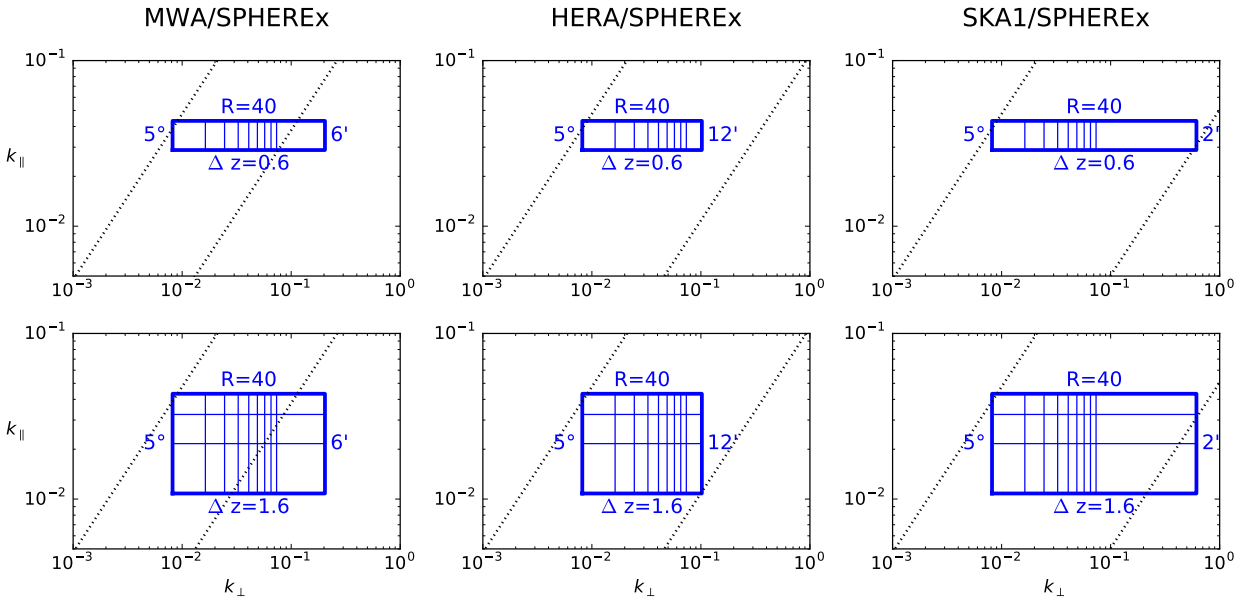

Fig. 1.— aoeuaoeuaoeu

4. Discussion

A. Power spectrum of photon shot noise

In Sec. **??** we measure the maximum airglow to be $I_{\rm air} = 5 \times 10^3$ kJy/sr, and in this appendix we calculate the power spectrum of this photon shot noise. We must observe that the mean number of photons collected by a pixel during each observation is $\langle N_{\rm ph} \rangle = I_{\rm air} A t_{\rm int} \Delta f d\theta^2 / hf$, where $A = (0.5\,{\rm m})^2$ is the collecting area of ATLAS, $t_{\rm int} = 30\,{\rm sec}$, Δf and f are the frequency bandwidth and center frequency of I band, and $d\theta$ is the pixel size. The passband has $\Delta\lambda = 150\,{\rm nm}$ and $\lambda = 800\,{\rm nm}$.

The shot noise contribution to the power spectrum is given by

$$C_{\rm IR,shot}(\vec{\ell}) = \left\langle \left| \sum_{m,n} I_{\rm shot}(m,n) e^{-2\pi i(ma+nb)/N} \right|^2 \right\rangle \frac{d\theta^2}{N^2} \tag{A1}$$

where $I_{\rm shot}(m,n) \equiv I(m,n) - \langle I(m,n) \rangle$ denotes the photon shot noise contribution to pixel (m,n), and N is the number of pixels on each side of the square image. Then using the fact that the shot noise is uncorrelated between different pixels, we find

$$C_{\rm IR,shot}(\vec{\ell}) = \sum_{m,n} \langle I^2_{\rm shot}(m,n) \rangle \frac{d\theta^2}{N^2} \tag{A2}$$

Note that $I(m,n) = N_{\rm ph}(m,n) hf / \Delta f A t_{\rm int} d\theta^2$ and $\langle N^2_{\rm ph} \rangle = \langle N_{\rm ph} \rangle$, so we have

$$C_{\rm IR,shot}(\vec{\ell}) = \langle N_{\rm ph} \rangle \left(\frac{hf}{\Delta f A t_{\rm int} d\theta^2} \right)^2 d\theta^2 \tag{A3}$$

$$C_{\rm IR,shot}(\vec{\ell}) = \frac{I_{\rm air} h\lambda}{\Delta\lambda A t_{\rm int}} \tag{A4}$$

NOTE THAT $C_{\rm shot}$ DECREASES WITH BINNING IN THE CROSS SPECTRUM, BUT NOT IN THE AUTO SPECTRUM!!!!!!!!!!!!!!!!!!!!!!!!

B. Relation between the power spectrum of image cubes and broadband images

NOTE THAT THIS ONLY HOLDS FOR LARGE ELL OVER A SMALL FIELD OF VIEW

We focus in this paper on the spherical power spectrum of broadband images, C_ℓ, instead of that of image cubes, $P(\vec{k})$, as 21 cm observations have focused on. Here we work out the relation between the two to facilitate comparison with past 21 cm power spectrum results. In particular, we calculate the scaling factor B relating the purely transverse modes of the power spectrum

$P(k_\perp, k_\parallel = 0)$ of a image cube $I(\theta_x, \theta_y, f)$ to the spherical power spectrum of a broad band image C_ℓ as

$$P(k_\perp, k_\parallel = 0) = BC_{\ell(k_\perp)} \tag{B1}$$

Using the fourier transform convention discussed in Sec. 2, the left side of the equation is given by

$$P(k_\perp, k_\parallel = 0) = \frac{1}{N_\perp^2 N_\parallel dV} \langle |\tilde{I}(k_x, k_y, k_\parallel = 0)|^2 \rangle \tag{B2}$$

where $N_\perp \equiv N_x = N_y$ is the number of pixels in each of the two transverse dimensions of the image cube, and $N_\parallel$ is the number of pixels in the line of sight (ie, frequency) dimension. The comoving pixel volume is $dV = (D_c d\theta)^2 (\Delta D_c / N_\parallel)$, where D_c is the line of sight comoving distance from the present day to the center of the cube, and ΔD_c is the comoving line of sight thickness of the cube. Lastly, recall that $k_\perp$ is related to k_x and k_y as $k_\perp = \sqrt{k_x^2 + k_y^2}$.

Now substituting the definition of the fourier transform, we find

$$P(k_\perp, k_\parallel = 0) = \frac{1}{N_\perp^2 N_\parallel dV} \left\langle \left| dV \sum_{\theta_x, \theta_y, f} I(\theta_x, \theta_y, f) e^{iD_c(k_x\theta_x + k_y\theta_y)} \right|^2 \right\rangle \tag{B3}$$

Simplifying and writing this in terms of the broadband image $I_{\Delta f}(\theta_x, \theta_y) \equiv \frac{1}{N_\parallel} \sum_f I(\theta_x, \theta_y, f)$, we find

$$P(k_\perp, k_\parallel = 0) = (D_c^2 \Delta D_c) \frac{d\theta^2}{N_\perp^2} \left\langle \left| \sum_{\theta_x, \theta_y} I_{\Delta f}(\theta_x, \theta_y) e^{iD_c(k_x\theta_x + k_y\theta_y)} \right|^2 \right\rangle \tag{B4}$$

Now denote $k_x = a \cdot dk$, $k_y = b \cdot dk$, $\theta_x = m \cdot d\theta$, and $\theta_y = n \cdot d\theta$, where $dk = 1/N_\perp D_c d\theta$.

$$P(k_\perp(\ell(a,b)), k_\parallel = 0) = (D_c^2 \Delta D_c) \frac{d\theta^2}{N_\perp^2} \left\langle \left| \sum_{m,n} I_{\Delta f}(m, n) e^{2\pi i(am + bn)/N_\perp} \right|^2 \right\rangle \tag{B5}$$

Comparing with Equations 5, 6, and 7, we see that $B \equiv P(k_\perp, k_\parallel = 0)/C_{\ell(k_\perp)} = D_c^2 \Delta D_c$ and $\ell = D_c k_\perp$.

REFERENCES

Ali, Z. S., et al. 2015, The Astrophysical Journal, 809, 61

Alvarez, M. A., Finlator, K., & Trenti, M. 2012, The Astrophysical Journal Letters, 759, L38

Atek, H., et al. 2015, The Astrophysical Journal, 814, 69

Beardsley, A. P., Morales, M. F., Lidz, A., Malloy, M., & Sutter, P. M. 2015, ApJ, 800, 128

Beardsley, A. P., et al. 2016, ArXiv e-prints

Bouwens, R. J., et al. 2011, The Astrophysical Journal, 737, 90

Bowman, J. D., et al. 2013, PASA, 30, e031

Bradley, L., et al. 2012, The Astrophysical Journal, 760, 108

Cooray, A., et al. 2012, Nature, 490, 514

Dark Energy Survey Collaboration et al. 2016, MNRAS, 460, 1270

DeBoer, D. R., et al. 2016, ArXiv e-prints

Dillon, J. S., et al. 2015, Phys. Rev. D, 91, 023002

Doré, O., et al. 2014, ArXiv e-prints

—. 2016, ArXiv e-prints

Dunlop, J. S., et al. 2013, Monthly Notices of the Royal Astronomical Society, 432, 3520

Ewall-Wice, A., Dillon, J. S., Mesinger, A., & Hewitt, J. 2014, MNRAS, 441, 2476

Fernandez, E. R., Zaroubi, S., Iliev, I. T., Mellema, G., & Jelić, V. 2014, MNRAS, 440, 298

Furlanetto, S., Oh, S., & Briggs, F. 2006, Physics Reports, 433, 181

Furlanetto, S. R., & Lidz, A. 2007, The Astrophysical Journal, 660, 1030

Gardner, J. P., et al. 2006, Space Science Reviews, 123, 485

Hall, P. J. 2005, The Square Kilometre Array: An Engineering Perspective

Helgason, K., Ricotti, M., Kashlinsky, A., & Bromm, V. 2016, MNRAS, 455, 282

Heneka, C., Cooray, A., & Feng, C. 2016, ArXiv e-prints

Illingworth, G. D., et al. 2013, The Astrophysical Journal Supplement Series, 209, 6

Jacobs, D. C., et al. 2015, ApJ, 801, 51

Kashlinsky, A., Arendt, R. G., Ashby, M. L. N., Fazio, G. G., Mather, J., & Moseley, S. H. 2012, ApJ, 753, 63

Kashlinsky, A., Arendt, R. G., Mather, J., & Moseley, S. H. 2005, Nature, 438, 45

—. 2007, ApJ, 657, L131

Lidz, A., Zahn, O., Furlanetto, S. R., McQuinn, M., Hernquist, L., & Zaldarriaga, M. 2009, ApJ, 690, 252

Mao, X.-C. 2014, ApJ, 790, 148

Morales, M. F., & Wyithe, J. S. B. 2010, Annual Reviews of Astronomy and Astrophysics, 48, 127

Park, J., Kim, H.-S., Wyithe, J. S. B., & Lacey, C. G. 2014, MNRAS, 438, 2474

Parsons, A. R., et al. 2014, The Astrophysical Journal, 788, 106

Planck Collaboration et al. 2016, A&A, 594, A13

Pober, J. C., et al. 2015, The Astrophysical Journal, 809, 62

Pritchard, J. R., & Loeb, A. 2012, Reports on Progress in Physics, 75, 086901

Ricker, G. R., et al. 2014, in Proc. SPIE, Vol. 9143, Space Telescopes and Instrumentation 2014: Optical, Infrared, and Millimeter Wave, 914320

Robertson, B. E., et al. 2013, The Astrophysical Journal, 768, 71

Schmidt, K. B., et al. 2014, The Astrophysical Journal, 786, 57

Silva, M. B., Santos, M. G., Gong, Y., Cooray, A., & Bock, J. 2013, ApJ, 763, 132

Spergel, D., et al. 2013, ArXiv e-prints, 190

Thacker, C., Gong, Y., Cooray, A., De Bernardis, F., Smidt, J., & Mitchell-Wynne, K. 2015, ApJ, 811, 125

Tingay, S. J., et al. 2013, PASA, 30

Tonry, J. L. 2011, PASP, 123, 58

Tonry, J. L., et al. 2012, ApJ, 750, 99

Trenti, M., et al. 2011, The Astrophysical Journal, 727, L39

Zackrisson, E., Rydberg, C.-E., Schaerer, D., stlin, G., & Tuli, M. 2011, The Astrophysical Journal, 740, 13

Zemcov, M., et al. 2014, Science, 346, 732

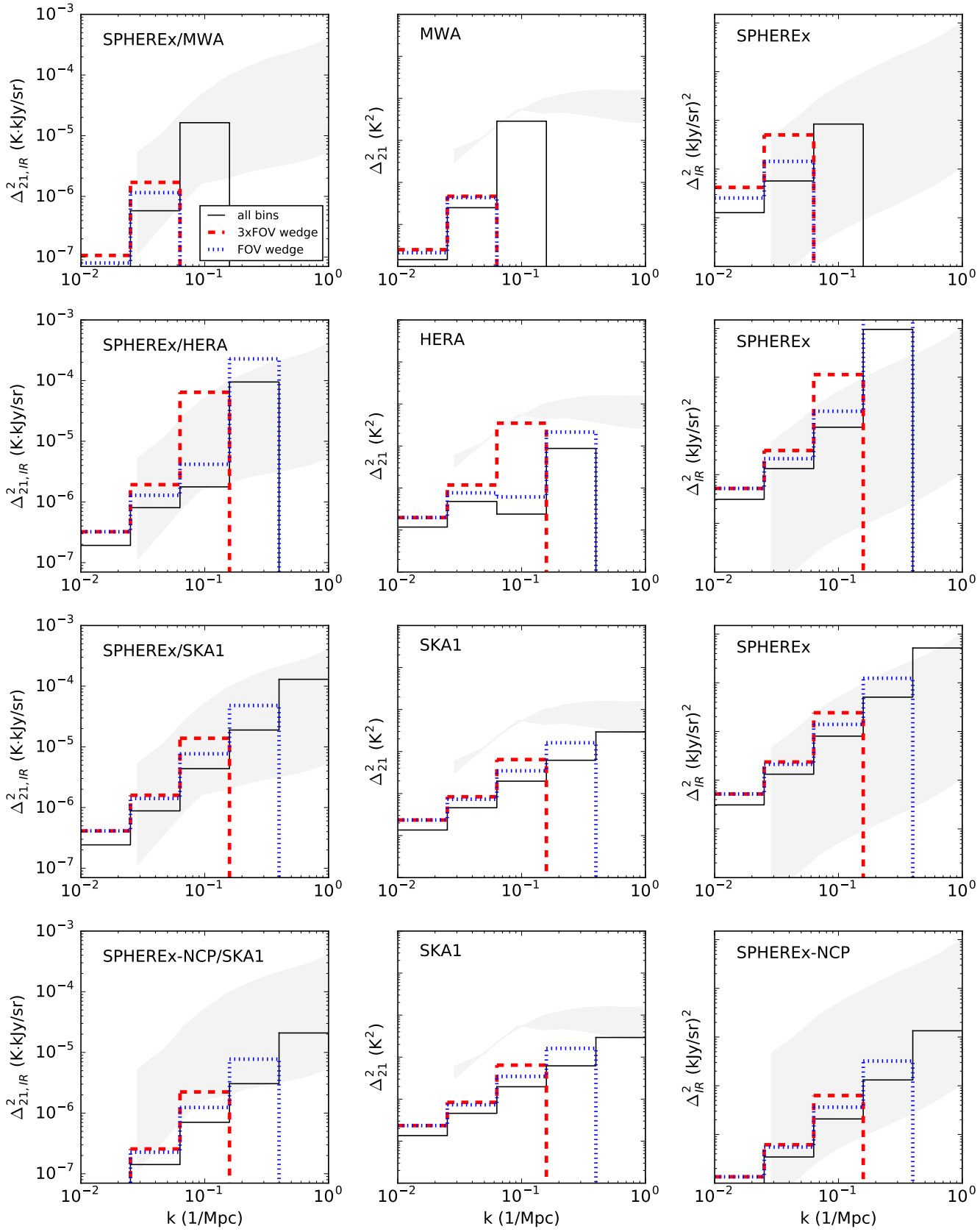

Fig. 2.— aoeuaoeuaoeu